New Journal and we have not received input yet 24 (2020) 100199

Contents lists available at ScienceDirect

FlatChem

journal homepage: www.sciencedirect.com/journal/flatchem

Ultrasonic doping and photo-reduction of graphene oxide films for flexible and high-performance electrothermal heaters

Sandra A.N. Tembei [a,*], Ahmed M.R. Fath El-Bab [b], Amr Hessein [c,e], Ahmed Abd El-Moneim [a,d,e]

[a] Department of Materials Science and Engineering, Egypt-Japan University of Science and Technology, New Borg El Arab City, Alexandria 21934, Egypt
[b] Department of Mechatronics and Robotics, Egypt-Japan University of Science and Technology, New Borg El Arab City, Alexandria 21934, Egypt
[c] Department of Mathematical and Physical Engineering, Faculty of Engineering (Shoubra), Benha University, Cairo 11614, Egypt
[d] School of Basic and Applied Science, Egypt-Japan University of Science and Technology, New Borg El Arab City, Alexandria 21934, Egypt
[e] Graphene Center of Excellence for Energy and Electronic Applications, Egypt-Japan University of Science and Technology, New Borg El Arab City, Alexandria 21934, Egypt

ARTICLE INFO

Keywords:
Ultrasonic doping
Nitrogen-doped graphene
Laser writing
Electrothermal heaters
Wearable electronics

ABSTRACT

Thermotherapy has emerged as one of the most promising treatments for arthritis, a prevalent, crippling, painful bone disease. This demands more flexibility, energy-efficiency, safety, and light-weight in thermotherapy packs and hot clothing. Heteroatom doping is a metal-free, cost-effective way to improve carrier concentration and hence electrical and thermal conductivity in reduced Graphene Oxide (rGO) thus rendering it suitable for wearable joule heaters. However, the current doping techniques result in complex chemical structures that hinder phonon propagation and suffer other problems such as low yield, low scalability, and rigidity of the final product. Here, we disclose a novel and facile, low-temperature technique for nitrogen doping and photoreduction of graphene oxide (GO) films for high-performance, flexible graphene-based electrothermal heaters. The nitrogen atoms are introduced into the GO lattice with the aid of ultrasonic power in a wet chemical doping phase and maskless, automated, rapid CO_2 laser scanning is used for the concurrent removal of oxygen-containing functional groups and the rearrangement of nitrogen atoms in the graphene lattice. X-ray Photoelectron Spectroscopy (XPS) studies reveal up to 5.43% nitrogen dopant concentration with a high carbon to oxygen ratio of 16, while Raman studies uniquely show improved atomic ordering with I_D/I_G ratio of 0.51 in the nitrogen-doped Laser reduced graphene oxide (N-LrGO) films. The fabricated N-LrGO heater has a sheet resistance of 26 O/sq. and attains a higher steady-state temperature of up to 245.7 °C at a low driving voltage of 9 V with a low power demand of 0.7 Wcm^{-2} and a heating rate of 103 °C/s. Its excellent temperature distribution and high flexibility join with the scalability of the preparation technique to demonstrate great potential for its incorporation with next-generation wearable electronics powered by low voltage portable energy storage devices.

1. Introduction

Electrothermal heaters are resistive structures capable of self-heating by a joule effect wherein electrical energy is transduced to thermal energy [1]. Modern times have seen an ever-increasing demand for better performances in electrothermal heaters in terms of transduction efficiency, flexibility, weight, and power management [1]. Moreover, wearable applications such as hot clothing, thermotherapy packs, and other healthcare appliances make an extra demand for flexibility, stretchability, and energy savings in the next generation electrothermal heaters. The quest to satisfy all these performance features explains why flexible thin-film heaters (TFH) have gained substantial research grounds in recent years [1–8].

Low heater resistance allows for high steady-state temperatures to be attained at relatively lower driving voltage. This renders the heater highly efficient in its function as an energy transducer [1]. Many research efforts have already been invested in the line of providing reliably innovative, flexible heating solutions. Some of these solutions include the preparation TFH from metal nanoparticles and nanowires [9–11], carbon nanotubes (CNT) [2], and graphene [12] on flexible or even stretchable substrates [13,14]. Embedding metal nanostructures [8,15], CNT [16], or reduced graphene oxide (rGO) [17] within conductive or non-conductive polymers matrices have also been proposed.

* Corresponding author.
E-mail address: tembei.sandra@ejust.edu.eg (S.A.N. Tembei).

https://doi.org/10.1016/j.flatc.2020.100199
Received 11 August 2020; Received in revised form 24 September 2020; Accepted 26 September 2020
Available online 24 October 2020
2452-2627/© 2020 Published by Elsevier B.V.

Along with poor adhesions to polymer substrates [6], metals nanostructures and CNT have proved capable of penetrating the human skin, which may yield toxic effects and are thus categorized as not suitable for wearable applications [18]. Moreover, at high temperatures, they also suffer contamination due to oxidation at the particle junctions. This increases their resistivity, thus deteriorating their performance [5]. As a result, there has been a shift in attention toward highly conductive noble metals such as gold and silver, wherein their nanoparticles have been embedded in transparent polymer matrices to form high performance transparent flexible heaters [9,10]. However, the high cost of these precious metals makes them unattractive for wearable applications such as hot clothing, and thermotherapy packs wherein transparency is not needed.

Overall, the potentially low cost, lightweight, high electrical, and thermal conductivity of carbon-based materials such as graphene makes it a suitable candidate for joule heaters [5]. This makes graphene preparation routes that arrive at flexible heaters with high-performance features of paramount importance. Chemical exfoliation of graphite into GO, followed by reduction to rGO is one the most popular processing routes in research today because of its high yield and great potential for scalability [19]. Laser scribing has shown to be a chemical-free, rapid, low-temperature method to reduce GO deposited on flexible polymer substrates while affording the possibility for patterning for various applications [20–26] and the doping in the presence of precursor molecules [27–30]. Photo-irradiation has also been used to induce graphene for polyimide films [3,31] and from coal [32] via laser scribing. The heaters from laser-induced graphene (LIG) [3] showed excellent performance. However, they had slow heating rates and suffered degradation within extended periods of high applied power [3]. Zhang et al. [33] prepared flexible pattered heaters from Laser reduced graphene oxide (LrGO), which attained as a steady-state temperature of up to 247.3 °C at 18 V applied voltage. However, the heaters needed a longer response time of 20 s. Lin et al. [5] added silver nanoparticles to the GO films before laser reduction in attempts to build in conductive bridges between the graphene sheets in the c-direction. The heaters prepared from this nanocomposite attained a steady-state temperature of up to 229 °C after 5 s of applying 18 V. Even though the response time of these heaters were improved, their reliance upon high concentrations of costly precious metals make these films financially unattractive for large-scale wearable electronics. Also, more research efforts geared towards lowering the driving voltages of these flexible heaters are still necessary to render them compatible with portable electrochemical power sources.

Furthermore, doping graphene with elements such as boron, nitrogen, and sulfur has been proposed as a metal-free means of increasing charge carrier concentration [34], thus improving conductivity. Various methods have already been established for doping graphene, which can be separated into two categories. Firstly, the in-situ approaches, such as introducing the dopant atoms during graphene deposition by using CVD [28,35–37]. The second approach includes post-treatment methods of GO, such as hydrothermal methods [38], thermal annealing in the presence of dopant molecules [39], wet chemical methods [40], with heteroatom precursors [34]. While the in-situ approaches suffered low yield and high cost, the post-treatment methods involve harsh processing conditions incompatible with the use of flexible substrates, and theses procedures are too complex to industrialize. Besides, these doping techniques result in excessive lattice defects in the 2D structures which inhibit the propagation of phonons in the lattice. While electrons still can jump over minor vacancy and substitutional defects, phonons do not.

Consequently, the mean free path for phonons is much shorter than that for electrons. High electron density in the π^*state is just as relevant as a high degree of atomic ordering in electrothermal materials for adequate heat generation and the propagation of the generated heat, which occurs principally by the movement phonons in carbon-based materials [41]. For, joule effect is caused by the inelastic collisions between phonons and electrons in a material when a potential difference is applied [42]. This means that even though doping represents a low cost, metal-free, means to improve upon the electrical and electrochemical properties of graphene, more efforts are still required to improve upon the electrothermal behavior of doped graphene-based materials and to render them more compatible with flexible substrates.

In this work, present a novel low-temperature doping and reduction technique in which nitrogen dopants are driven into the graphene lattice in a wet chemical process with the aid ultrasonic cavitation energy and further processed by maskless, automated, rapid laser irradiation. Unlike other doping techniques, this method uniquely preserves order in the sp^2 network of the graphene sheets while a high dopant concentration is attained. This not only allows for large amounts of heat to be generated by the heaters but also offers the doped films a larger capacity to propagate the generated heat. Consequently, a significant improvement in electrical and electrothermal behavior was observed in comparison with the undoped LrGO films. The low-temperatures applied in this approach contribute to its scalability and compatibility with flexible polymer substrates. This paper is structured as follows. In Section 2 of the article, the fabrication and characterization methods are described along with the performance measurement procedure. The evolution of chemical structure is presented in the first subsection of Section 3. A second subsection describes the electrical and transient electrothermal performance of the nitrogen-doped graphene-based heater while benchmarking it against other heaters presented in previous works. Thermal stability, robustness, and potential applications of the heaters are examined in a later subsection of Section 3, while Section 4 summarizes our key findings.

2. Materials and methods

2.1. Materials

Extra-pure graphite powder with 5–20 μm grain size and 30% Ammonia solution [NH_4OH] were purchased from Fisher Scientific, UK. Urea granules [CH_4N_2O] were obtained from Sigma Aldrich, Germany. All the other chemicals were reagent grade and used as received without any additional purification. Polyethylene Terephthalate (PET) substrates with 75 μm thickness were locally sourced.

2.2. Preparation of N-GO films

Graphite oxide was prepared according to the modified Hummer method [43,44]. 10 g Graphite was oxidized with 60 g of $KMnO_4$ in a 98.9% HNO_3/H_2SO_4 acidic medium for 4 days after which the reaction was neutralized with 40 ml of 30% H_2O_2. The resulting graphite oxide flakes were washed repeated with 70% HCl and distilled water and dried and 60 °C for 48.0 h. GO solution with a concentration of 4 mg/ml was prepared by dispersing and exfoliating graphite oxide flakes in distilled water by vigorous stirring, bath sonication for 1.0 h, followed by stronger probe sonication for 3.0 h in an ice bath. Nitrogen-doped GO (N-GO) was prepared by adding the nitrogen source directly into the GO solution. 30% Ammonia solution was added at a volume ratio of 0.1:1 to the graphite oxide suspension before bath sonication for 1.0 h. Before final strong bath sonication for 3.0 h, urea granules were then added in at mass ratios of 0.4:1, 0.2:1, and 0:1 (these mass ratios are based on the initial dry mass of graphite oxide) for the samples denoted hereafter as $N_{0.4}$, $N_{0.2,}$ and N_0 respectively. The removal of unexfoliated graphite GO, and N-GO solution was subsequently done by centrifugation at 4000 rpm for 20 min and independently drop cast (0.27 ml/cm^2) on PET substrates films and set to dry for 48 h to form the GO and N-GO films respectively.

2.3. Laser irradiation and heater fabrication

To produce LrGO and the nitrogen-doped laser reduced graphene

oxide (N-LrGO) films, the GO and N-GO films were subjected to laser irradiation. The VLS 2.30 Universal laser system was employed. In this automated step, a continuous wave CO_2 laser with a wavelength of 10.64 μm was rail-guided to scan an area of 25 × 20 mm^2 was scanned into both the GO and N-GO films. Photo-irradiation was carried out at 2.7 W laser power, 58.3 mm/s scan speed, and 125 pulses per Inch to form the LrGO and N-LrGO films, respectively. Better performance was obtained by scanning the same area twice [5]. To minimize the coffee ring effect and obtain better control of the film thickness, laser scanning was done 1 cm away from the edges of the as-cast films. The heaters were then fabricated by, attaching strips of copper tape to both edges of the LrGO and N-LrGO films to form the electrical terminals. This was closely followed by applying silver paste across the junctions to reduce contact resistance. The final effective area of the heaters we maintained at 20 × 20 mm^2 Fig. 1(b). The heaters were fabricated on hollow acrylic supports, which allowed for heat dissipation on both sides of the heater, as shown in Fig. 1(b).

2.4. Transient electrothermal performance measurements

With a direct current (DC) power supply step voltages were applied across the copper terminals of the heaters. The transient behavior was tracked by recoding the evolution of average temperatures of the heater with time. The average temperatures were observed by thermal imagery using the NEC TH9260 Infrared camera.

2.5. Bending test

A bending system was assembled to investigate the robustness of the heaters. The bending system was motorized and electronically controlled with a simple counting software code. It consisted of a motor, a motion transfer sub-system, a static clamp, and a moving clamp sliding of over rail guide, as shown in Fig. 1(c). The motor was programmed to perform 15 sets of 200 bending cycles for each heater, and the resistance of the heater was measured after each set. The test heater was fixed within the static clam on one side and the movable clamp on the opposite side. A bending angle of 135° was applied in every cycle. More details of all other characterization techniques can be found in the Electronic Supporting Information (ESI).

3. Results and discussion

3.1. Structure and morphology

The XRD patterns of GO, LrGO, N-GO, and N-LrGO are shown in Fig. 2(a). The diffraction peak associated with the (002) plane of the graphene lattice, progresses from about 10.4° in GO and 10.26° in N-GO to 26.80° in LrGO and 24.46° in N-LGO. This signifies an increase in interlayer spacing ($d_{(002)}$) from 0.848 nm in GO to 0.861 nm in N-GO, and the increase can be attributed to the incorporation of larger nitrogen functional groups [45] into the graphene lattice. Similarly, the corresponding decrease in $d_{(002)}$ from of 0.848 nm in GO and 0.861 nm in N-GO to 0.348 nm in LrGO and 0.3644 nm in N-LrGO can be attributed to the removal or processing of oxygen and nitrogen functional groups during the photo-irradiation process.

Additionally, the broad peak around 25.28° in the N-GO diffraction pattern can be associated with the (200) plane of non-functionalized (reduced) regions of the nanostructure. This shows that partial reduction is also accomplished during the wet chemical doping process[34] before laser irradiation.

Fig. 2(b) shows the Raman shifts for GO, NGO, and N-LrGO, ranging from 1000 to 3500 cm^{-1}. Three of the characteristic Raman modes for graphene-based materials were observed. The first is the D mode; occurring at a frequency of 1342 cm^{-1}, signifies the vibrations coming from lattice defects. The second peak is the G mode, occurring at about 1586 cm^{-1}, represents the aggregate of the bond vibrations from the defect-free (graphitic) zones [46,47]. The last 2D vibration mode was only observed in the N-LrGO spectrum at a frequency of 2680 cm^{-1}, and

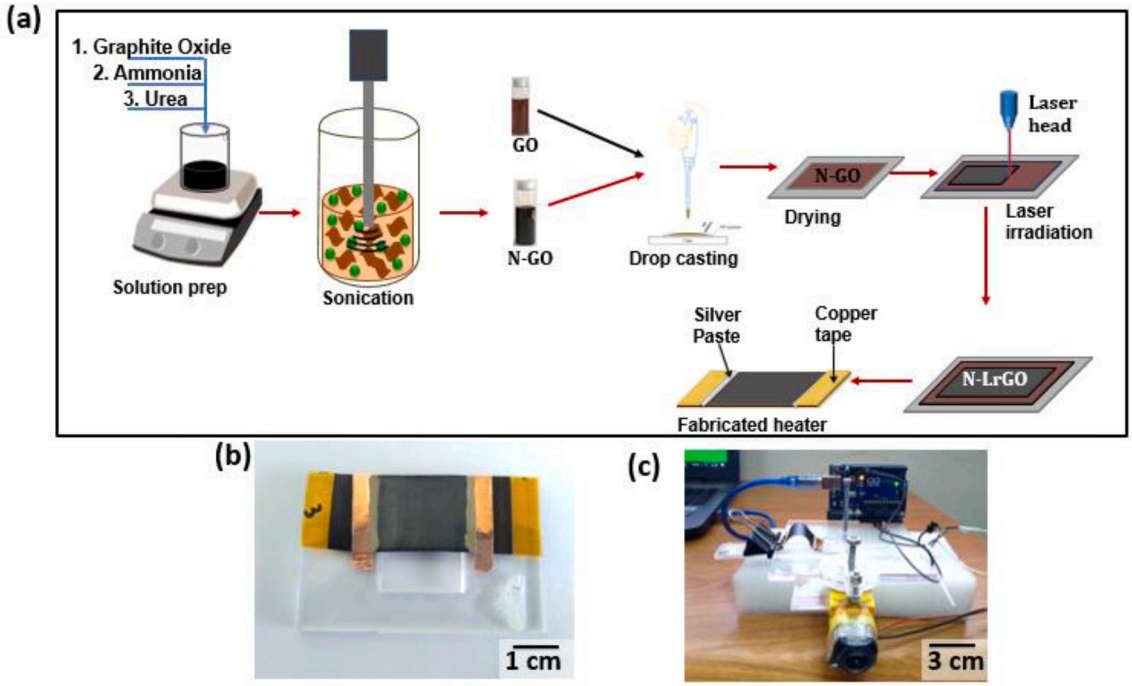

Fig. 1. Sample preparation and flexibility testing. (a) Schematic of N-LrGO film preparation and heater fabrication processes; dopant precursors are added to the graphite oxide suspension and the sonication probe releases bursts of cavitation energy to drive the nitrogen dopants into the GO sheets in the liquid phase; the N-LrGO film is laserwritten into to the N-LrGO film; copper terminals are planted on opposite sides of the N-LrGO film and electrically sealed in with a silver paste to build the heaters (b) Fabricated heater; heater is mounted on a hollowed acrylic support. (c) Bending system in operation; heater is dismounted from the acrylic support and held between opposite clamps of the bending unit.

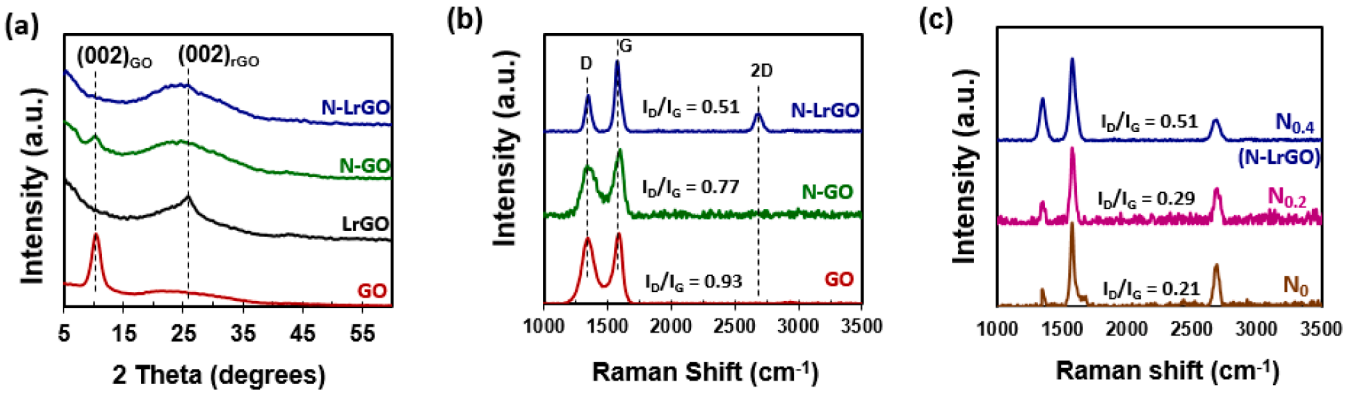

Fig. 2. Structural analyses. (a) XRD spectra of GO, LrGO, N-GO, and N-LrGO; the peak position of the (0 0 2) plane shifts from left in GO and N-GO to right in LrGO and NLrGO to indicate good reduction. (b) Raman spectra of GO, N-GO, and N-LrGO; (c) Raman Spectra of N-LrGO, $N_{0.2}$, N_0; $N_{0.2}$ and N_0 are the samples prepared with less urea; D represents the defect band, G, the graphitic band and 2D, the second-order harmonic of the G band; I_D/I_G stands for the ratio of the D and G band intensities; a smaller ratio indicate a lower defect density and better lattice ordering.

it represents the second-order harmonic of the phonon vibrations coming from the sp^2 domain [48]. The I_D/I_G ratio, estimated as the ratio of the area enveloped by the D band to that covered by G-band, indicates the degree of atomic ordering in the graphene lattice. The decrease I_D/I_G ratio from 0.93 in GO to 0.76 in N-GO and finally to 0.51 in N-LrGO indicates that partial reduction of the GO takes place in the wet chemical phase, and further abatement of lattice defects occurs during laser irradiation. This is caused by the chemical and photothermal removal of both oxygen and nitrogen functional groups as indicated by the XRD data. The lower I_D/I_G ratios in samples $N_{0.2}$ (0.29) and N_0 (0.21) owes to lower nitrogen content and thus fewer sp and sp^3 defects Fig. 2(c).

Furthermore, the result of the XPS studies of GO, LrGO, and N-LrGO are shown in Fig. 3. The wide spectra in Fig. 3(a,b,c) principally capture C1s at 284.2 eV, O1s at 532.0 eV and N1s at 399.4 eV [39]. These nitrogen related peaks seen this the wide GO and LRGO are largely composed of the Oxidized-N introduced by the nitric acid used in the graphite oxide preparation step [49]. This is characteristic of GO batches that employ the use of nitric acid in the modified Hummer preparation process [50]. The increase of the carbon to oxygen ratio from 2 in GO to 16 in both LrGO and N-LrGO further demonstrates the efficacy of this doping and reduction technique since a high nitrogen content of 5.43% is still maintained the N-LrGO film even after laser irradiation. This is a dual technical improvement not attained in previous related works [28,37,51,52] and other photoreduction techniques involving UV light [53] and sunlight [54] because GO reduction commenced in the wet chemical doping process and the high penetration depths afford by the high-intensity laser CW lasers. The C1s of LrGO and N-LrGO were expanded and deconvoluted, as shown in Fig. 3 (d,e). Deconvolution of the C1s peaks of LrGO fitted to 284.4 eV, 286.23 eV, and 288.56 eV, respectively attributed to the C═C bond in the sp^2 domain, the C-O-C of the epoxy-functional group, and to the C═O bond of carbonyl groups that persist after reduction [5]. The C1s N-LrGO were also fitted to

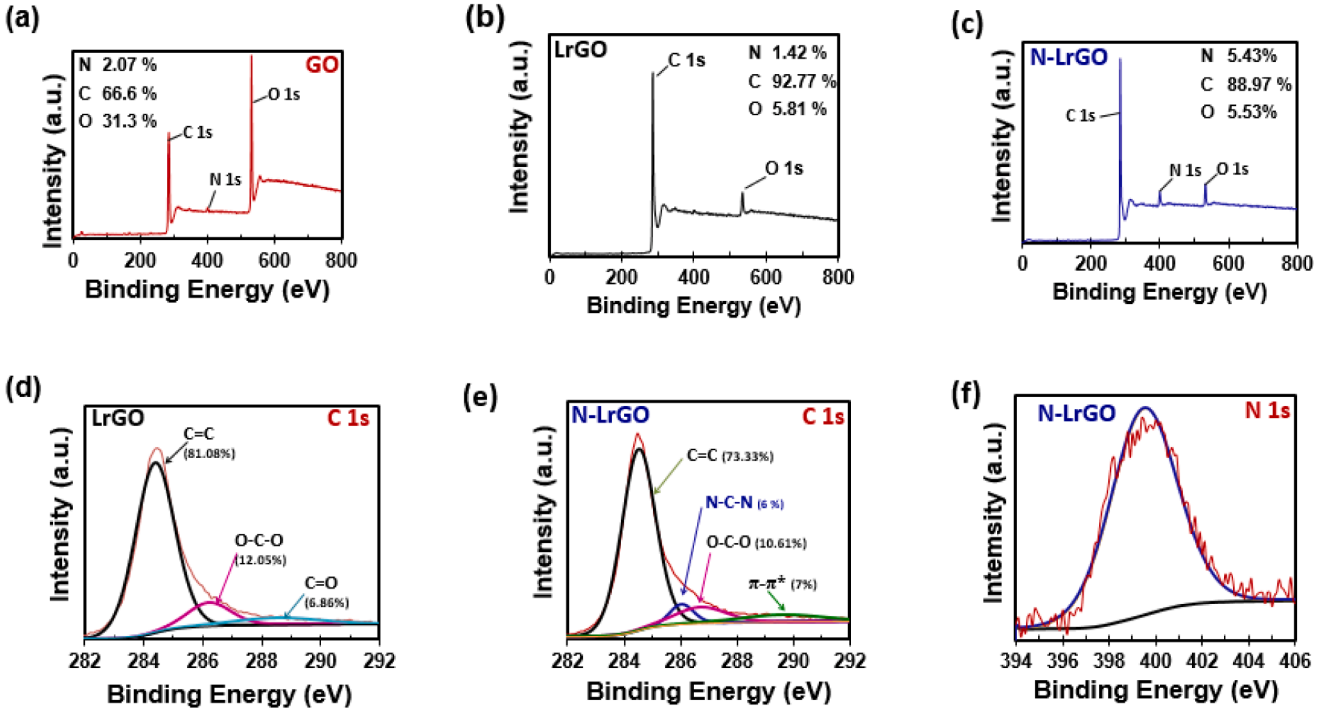

Fig. 3. XPS analysis. Wide XPS spectra of (a) GO, (b) LrGO, and (c) N-LrGO samples; elemental compositions are inserted. Deconvoluted XPS spectra for C1s in (d) LrGO, and (e) N-LrGO samples and (f) the N1s in N-LrGO sample; the bond proportion as inserted. A large percentage of the C1s in N-LrGO are sp2 bonded thus indicating good lattice ordering; the N1s of N-LrGO all assume a pyrrolic configuration.

284.52 eV for the C═C bond in the sp^2 domain, 286.03 eV for the C—N—C bond [28,39] the pyrrolic group, 286.7 eV for the C—O—C bonds in the epoxy groups, and finally, 289.64 eV attributed the resonance derived from photoelectron beam interactions with the π-π* electron transitions [3]. The π-π* peak is associated with why broad sp^2 clusters [34,55], which signifies a high degree of ordering in the N-LrGO nanomaterial. This is in good agreement with the low I_D/I_G ratio observed in the N-LrGO Raman shift. Nitrogen doping in alters the densities of state in the reduced materials thus making these π-π* transitions more detectible in the N-LrGO than in the LrGO. Fig. 3(f) shows the N1s in N-LrGO spectrum. The lone binding energy of 399.5 eV indicates that all the nitrogen atoms assume a pyrrolic configuration. The wide XPS spectra and N1s of the N-doped graphene prepared with less urea ($N_{0.2}$) and no urea (N_0), are shown in Fig. S1 in the ESI. The nitrogen content of $N_{0.2}$ is 2.25% while that of N_0 is 1.18%.

The FTIR spectra collected from the prepared samples are shown in Fig. 4(a) and all obtained peaks are assigned to the corresponding vibrational modes belonging to the existing function groups present in each sample. After careful consideration of the GO, N-GO, and N-LrGO spectra, the reactions possibly taking place in the wet chemical doping and laser reduction processes are proposed in Fig. 4 (b). With the heat energy released due to ultrasonic cavitation ($\Delta_{Cav.}$), the ammonia molecules make more energetic collisions with the carboxylic groups at the edges of the graphene sheets in a substitution reaction to form primary amides [56] (reaction (1),2), some of which may undergo resonance with the carbon atoms on the edge of the graphene sheets to form secondary amides (reaction (1)). This explains the apparition N–H stretches attributed to the presence of primary and secondary amides in the N-GO FTIR spectrum. The secondary amides undergo a decarbonylation reaction during laser irradiation to form either hydrogenated pyrrols(reaction (3)) or oxidized pyrrols (reaction 4) in the XPS spectra as the pyrrolic-N, Fig. 4(b). This explains the large reduction in the intensity of the N–H stretches belonging to the amide groups in the N-LrGO spectrum and the apparition of the C-N stretch at 1417.3 cm^{-1}.

Urea releases ammonia slowly into the reaction as the reaction progresses to continuously attack the carboxylic and hydroxyl groups [56]. We theorize that the cavitation energy released during the strong sonication step in the preparation process [57], induces the breakdown of the urea molecules while performing the intended exfoliation of graphite oxide sheets. Since the ammonia solution has a boiling point of only 24.9 °C, it vaporizes out the open reactor as much faster during probe sonication because of cavitation and heating. Consequently, doping and reduction are taken over by ammonia molecules coming from the slower break down of urea during the stronger ultra-sonication step. This explains why the samples with less and no urea $N_{0.2}$ and N_0 showed lower nitrogen content. This proves that urea is a better dopant source than ammonia using this cold open reactor technique. However, it was necessary to start the exfoliation process with ammonia to initiate a reduction of the GO as early on as possible. The breakdown of urea during the strong ultrasonic exfoliation step was too slow to accomplish this process. We also found that increasing the urea charge to the reactor did not increase the final dopant concentration by rather resulted in the recrystallization of the unreacted urea in the dried film. These large urea crystals, occurring as visible dendritic structures in Fig. S2 (a), undermined the flexibility of the films. $N_{0.4}$ was, therefore, the optimized feed proportion to circumvent this recrystallization phenomenon.

High-magnification TEM, images on the GO nanostructure, Fig. S3 revealed the typical corrugated structure of GO. This periodically folded morphology is attributed to the localized intrinsic strain induced by the introduction of oxygen functional groups on the graphene sheets [58]. A significant reduction in surface corrugation was noticed after laser reduction, as seen in the LrGO TEM image Fig. 5 (a). This is because most of the oxygen groups have been removed, thus releasing some strain. A similar observation was noticed in the case of N-GO and N-LrGO where N-GO showed more surface corrugation than N-LrGO sample. However, slightly more folding is observed in the N-LrGO nanostructure Fig. 5 (b–d) than in the LrGO nanostructure, as expected [59]. This is because the sp^3 bonded pyrrolic-N introduced into the basal plane are of dissimilar bond lengths with the sp^2 C–C. Consequently, this disrupts the planar structure of the graphene sheets [34], resulting in a slight

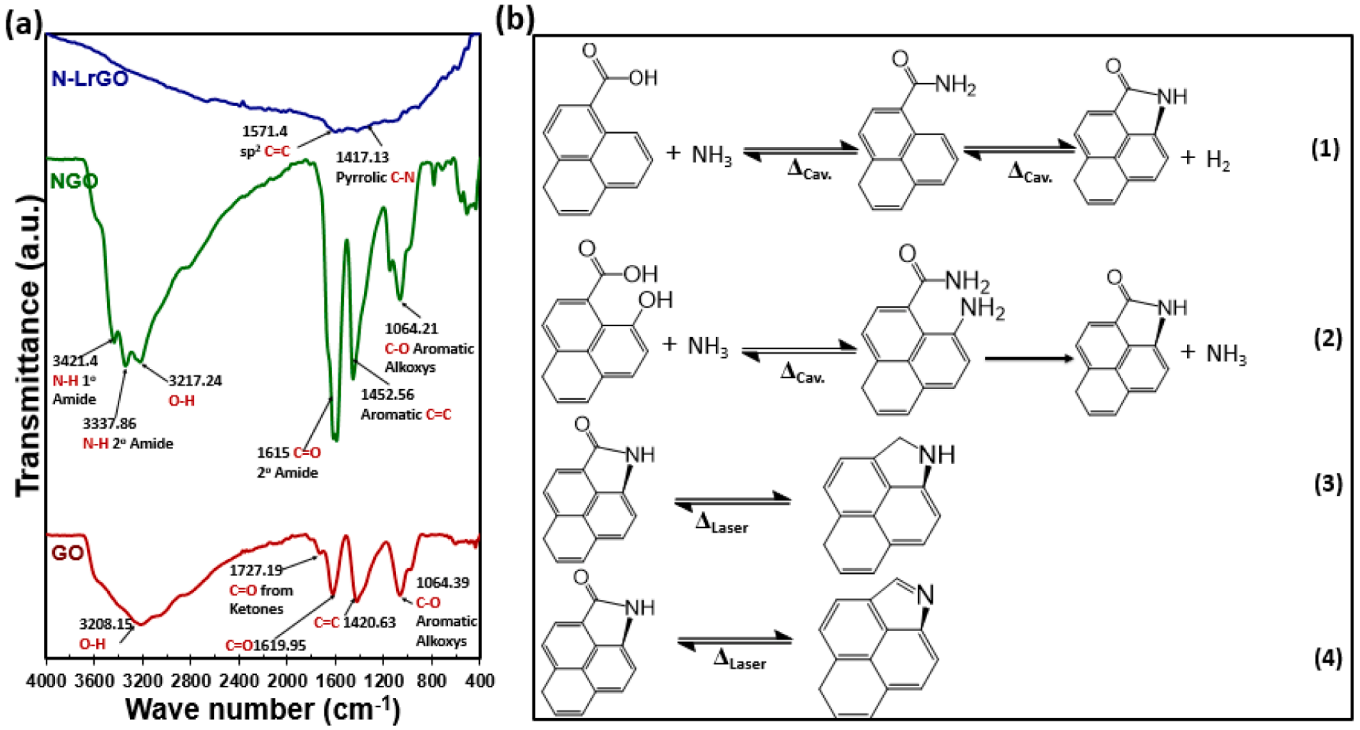

Fig. 4. Chemical analysis of the doping process. (a) FTIR spectra of GO, LrGO, N-GO, and N-LrGO; the bond stretches and vibration are identified and inserted. (b) Chemical reactions occurring in the wet chemical doping (1–2) and Laser irradiation (3–4) processes; reactions are proposed based on careful consideration of the FTIR and XPS analysis.

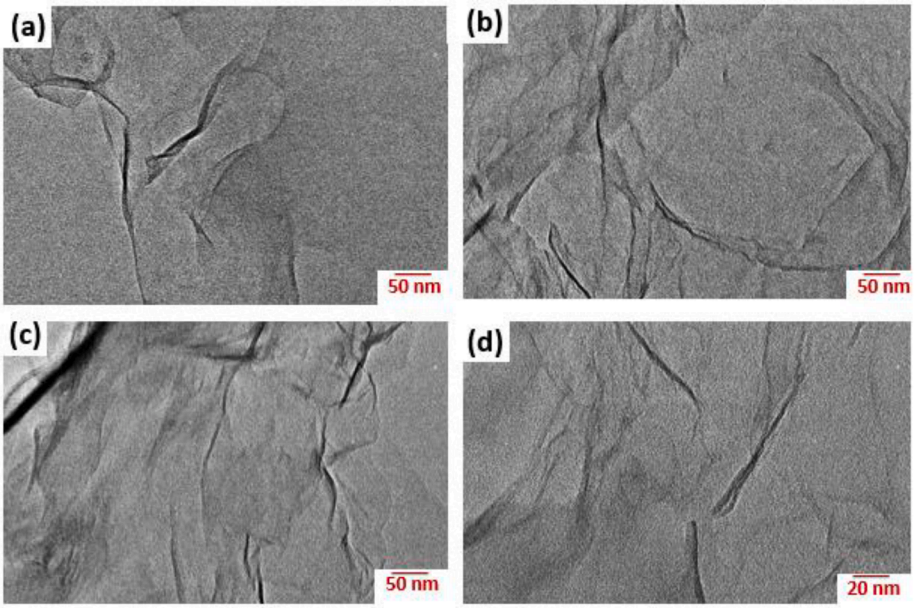

Fig. 5. TEM images of (a) LrGO and (b,c,d) N-LrGO; scale bars are inserted; both LrGO and N-LrGO lamellae show good continuity; the N-LrGO lamellae show more folds; a higher resolution image (d) equally reveals more surface corrugation.

increase in the surface corrugation.

3.2. Effect of N-Dopant on the electrical behavior of N-LrGO

The large oxygen-containing functional groups on the GO and the amides on the N-GO sheets along with sp^3-defects such epoxies, on both sides of the sheets act as points of excessive electron scattering [60] resulting in poor conductivity. Nevertheless, the laser-induced removal of the large oxygen functional groups in the GO and N-GO films alongside the decarbonylation of the amides in the N-GO results in the restoration of conducting domains. A sheet resistance (R_s) of 52 O/square and 26 O/square was measured for the LrGO and N-LrGO films, respectively. This 50% drop in R_s from LrGO to N-LrGO is attributed to the effect of nitrogen doping and is accounted for by three contributing factors, namely; an increase in carrier concentration, a drop in the fermi energy level, and an increase in interconnectivity between the N-LrGO sheets.

$$\sigma = \frac{ned}{mV_f} = \frac{1}{R_s t} \tag{1}$$

For a closer consideration of these factors, it is necessary to recall that the definition of conductivity, σ, in a conductive material is defined by Eq. (1), where; n is the number of charge carriers, e is the electronic charge, m is electronic mass, V_f is Fermi speed, and d is the mean free path. When hydrogenated, the pyrrolic-N takes on n-type behavior in graphene by contributing an extra 0.5 electron to the lattice thus improving carrier concentration (n) [61]. This implies that the high N-content of N-LrGO, may have caused a considerable increase in the charge carrier concentration. Also, the large π-π* transition band observed in the C1s on the N-LrGO XPS spectrum, Fig. 3(e) suggests a lowering of the fermi energy and hence the fermi speed, thus greatly contributing to the increased electrical conductivity probed by the decreased sheet resistance of the N-LrGO films. Finally, the pyrrolic-N groups at the edges of the N-LrGO sheets slightly disrupt the planar structure of the graphene sheets. They, therefore, cause the edges of the N-LrGO sheets to fold into the basal planes of their transversely located neighbors without the risk of restacking. This results in increase interconnectivity of the N-LrGO sheets in the C-direction, consequently increasing electron percolation [5,62,63] and hence improves conductivity. This is corroborated by the increase in surface corrugation observed in the TEM images of N-LrGO nanomaterial, Fig. 5(b–d). The I-V curves for LrGO and N-LrGO, Fig. S4 (a) in the ESI, confirm the Ohmic behavior of both materials.

3.3. Transient electrothermal behavior

The transient electrothermal behavior of the LrGO and N-LrGO heaters are shown in Fig. 6. Discrete DC voltages of 1.5–9 V were applied across the copper terminals of each heater, and the thermal responses were recorded with an infrared camera. All measurements were carried out under ambient conditions. When each potential difference was applied, a swift, monotonic temperature rise was observed in each case until the steady-state temperature was attained. The power was switched off after 50 s, and this was immediately followed by a swift drop in the temperature of the heaters till it returned to that of the room (20 °C). With step increments in the supply voltage, both LrGO and N-LrGO films also showed corresponding but unequal step increments in the steady-state temperature while maintaining synchronous behavior in regards to the response time. This is due to the non-linearity in the resistance–temperature relationship, which is typical of carbon-based electrothermal heaters [4,5,7]. From Fig. 6(a), the LrGO heater attained a steady-state temperature 154 °C after 10 s of applying 9 V voltage. With the N-LrGO device, Fig. 6(b), however, a much higher a steady-state temperature of 244 °C was attained after 10 s of applying the same 9 V potential difference. The comparison is well depicted in Fig. 6(c) wherein the effect of nitrogen doping is seen to produce a 60.6% increase in steady-state temperature at a constant voltage of 6 V. The $N_{0.4}$ samples showed the best electrothermal performance as it had the highest nitrogen content. An excellent temperature distribution can be observed in the thermal images of both LrGO and N-LrGO films since about 95% of the heater surfaces attained 90% of the maximum steady-state temperature.

The saturation temperature (T_{sat}) is proportional to the consumed power (P), $T \sim P$, which is defined as $P = V^2/R$. This implies the T_{sat} is, in turn, inversely proportional to the device resistance (R). Equation (2) is the parabolic relationship between T_{sat} and V in TFH [12] wherein h_c is the convective heat transfer coefficient, A_c is the area over which the heat is lost, and Δt is the time needed to arrive at the saturation temperature from an initial temperature T_i.

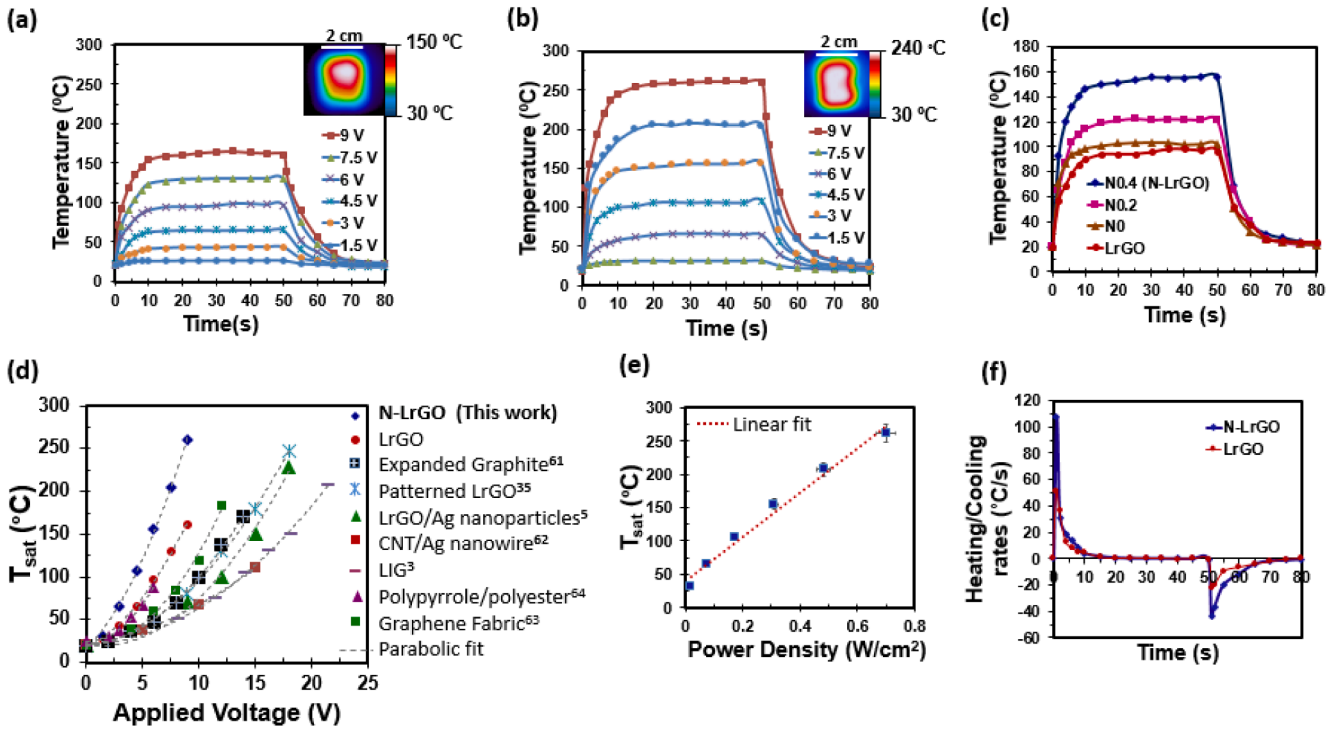

Fig. 6. Electrothermal analyses of LrGO and N-LrGO. Thermal response of (a) LrGO and (b) N-LrGO to different applied voltages; see inserted thermal images of the heaters taken at 9 V applied voltage showing good temperature distribution. (c) Comparison of thermal response of LrGO, N0, N0.2, and N-LrGO at 9 V supply; the N-LrGO shows the highest saturation temperature. (d) V-Tsat curves for N-LrGO, LrGO, and other carbon-based thin-film heaters recently proposed in the literature; the N-LrGO parabola rises fastest, indicating better energy transduction. (e) Relationship between saturation temperature with invested power in the N-LrGO heater; the linear fit indicates good heater controllability. (f) Heating and cooling rates LrGO and N-LrGO at 9 V supply voltage.

$$T_{sat} = \frac{V^2 \Delta t}{R h_c A_c} + T_i = \frac{P \Delta t}{hA} + T_i \quad (2)$$

Less sheet resistance in N-LrGO film explains this 60.6% gain in transduction efficiency over the LrGO film at 6 V, which is a measure of the gradients of the Voltage – T_{sat} plot. Fig. 6(d) shows that this gain gradually growing from 0% at 0 V to 61.3% at 9 V as the two parabolas converge at room temperature. Benchmarking this Voltage – T_{sat} plot against those of other carbon-based TFH such as LIG [3], patterned LrGO [33], LrGO/AgNP [5], Expanded graphite [64], CNT/AgNW [65] heaters, Graphene fabric [66], and Polypyrrole/Polyester [67], T_{sat} rises must faster with increasing voltage in the N-LrGO heater. This implies superior transduction efficiency was attained with the N-LrGO, which can be attributed to its low sheet resistance. This allows for large current density in the material when a voltage is applied.

While electrons can jump over minor vacancy and substitutional defects, phonons do not [41]. Consequently, the mean free path for phonons is much shorter than that for electrons. Since phonons play a major role in heat generation and propagation in carbon-based materials, their movement in the nanomaterials becomes an important factor to consider. In layered graphene-based materials, the thermal conductivity, k is defined by Eq. (3) [41].

$$k = c_v v_s l \quad (3)$$

where c_v, v_s, and l are the specific heat capacity per unit volume, speed of sound and the phonon mean free path. l is closely related to the degree of order in the graphene lattice; it is the dimension of the defect-free zones in graphene which increases with decreasing I_D/I_G Raman ratio. Therefore, the good atomic ordering in N-LrGO, as indicated by an I_D/I_G ratio of 0.51 allows for better phonon propagation in the 2D material thus improving the chances for inelastic collisions with electrons when a voltage is applied and resulting in more joule heating effect. This causes higher saturation temperatures to be attained in the film heaters with low driving voltages, resulting in a larger thermal potential to drive the generated heat.

Examining the power demand of a TFH is paramount importance in determining its applicability in wearable electronics wherein power management is of great concern. Fig. 6(e) shows the expected linear relationship between electric power consumption per cm^2 and T_{sat} attained at each step voltage. The linear relationship between power density and T_{sat}, which agrees with Equation (2), guarantees reliable power-dependent temperature control of the N-LrGO heater. This linear fit defines a low power demand of 30.07 W/m^2 °C which compares well with those recently reported for the LIG [3] (76.33 W/m^2 °C), patterned LrGO [33] (89.92 W/m^2 °C), few-layer graphene-FLG [68] (43.48 W/m^2 °C), Graphene/Polyurethane/cotton [66] (37.57 W/m^2 °C), graphene/Toulamine [69] (83.33 W/m^2 °C), Polypyrol/cotton [70] (29.65 W/m^2 °C), and Carbon fibre [71] (35.9 W/m^2 °C) heaters. This demonstrates a great potential for incorporation of the N-LrGO heating element into wearable electronics powered by portable, rechargeable or non-rechargeable energy storage components such as batteries and laser printed flexible supercapacitors [72] wherein power management is a great need.

High heating and cooling rates are some of the most attractive performance features of electrothermal heaters because they guarantee good controllability when incorporated with more complex automated electronic systems. Fig. 6(f) depicts the heating and cooling rates of the LrGO and N-LrGO films with time at 9 V. The LrGO film had a peak heating rate of 51.6 °C/s 9 V applied voltage, while the N-LrGO films had a peak heating rate of 107 °C/s. The value also competes well with those recently reported for other carbon-based TFHs such as LIG [3] (6.58 °C/s), LrGO/AgNP [5] (89.1 °C/s), Polypyrole/polyester [67] (3.90 °C/s), Graphene fabric [66] (8.4 °C/s), FLG (3.15 °C/s), Graphene/Polyurethane/cotton [66] (8.4 °C/s), rGO/WPU [73] (5.1 °C/s)and rGO/CNC/CDs composite♣ (44.9 °C/s) [74]. The N-LrGO heater had a peak cooling rate of 42 °C/s which to high enough to ensure good heat

dissipation when the heater is turned off.

3.4. Heater stability

To examine the thermal stability of the N-LrGO film thermal cycles were performed. Each cycle involved applying a 4.5 V voltage for 50 s and switching the heater off for 30 s. The N-LrGO heater showed great thermal cyclic behavior, as seen in Fig. 7(a) as the heating cycles remained almost identical right up to the 30th cycle. Fig. 7(b) shows thermal images capturing the evolution of the temperature distribution in N-LrGO film at different times in a single cycle. At 10 s, the entire area of the heater attained the saturation temperature of 96 ℃. When the heater is switched off at 50 s, the temperature was seen to drop to nearly room temperature in the 67th second. Saturation temperature stayed the same in each cycle thus proving its stability and reliable controllability if incorporated with more sophisticated electronic circuits. Fig. 7(c) captures a steady increase in resistance with repeated bending cycles and Fig. S4(b) shows IV curves before and after the bending cycles. A total increase of 3.35% was recorded after 3000 cycles, 75% of which occurred in the first 1000 cycles. However, this change in resistance was too small to make any considerable changes in the T_{sat} or temperature distribution. Fig. 7(d,e) show the N-LrGO film successfully folded at an oblique angle and a higher bending angle of 300°, respectively, with no visible damage to the film. This robust nature of the N-LrGO heater proves the compatibility of our wet chemical doping and laser reduction technique with the use of flexible polymeric substrates. The N-LrGO films also show excellent chemical stability, as their conductivities remained the same, even after 3.0 months of exposure to ambient conditions.

3.5. Potential applications

The prevalence of arthritis today has prompted lots of research into possible solutions [75]. Thermotherapy is one of the proposed treatment methods wherein the affected joint of a patient is kept at a temperature of about 70 °C to improve local blood circulation and relieve pain [76]. This is done using electronic hot packs. However, thermotherapy packages commercially available to medical treatment facilities suffer major setbacks such as heavyweight, high voltage requirement, and a lack of flexibility. These three factors render the patients extremely uncomfortable wearing these packs for extended periods [17]. This lightweight, efficient, flexible, and fast N-LrGO heater represents an excellent innovative solution to resolve these issues if integrated with thermotherapy packs and hot clothing. We applied a 1.5 by 2.5 cm^2 N-LrGO heater as a thermotherapy patch by wearing in on a human wrist slightly tilted sideways, to demonstrated flexibility in real-life application Fig. 8. The heater reached an average temperature of 65 °C at 4 V which is well within the safety limits for humans and permits extended periods of usage when powered by low-voltage energy storage devices such as Li-ion batteries and thin-film supercapacitors.

4. Conclusions

To sum up, we have successfully demonstrated a facile, scalable approach to the fabrication of high-performance flexible electrothermal heaters based on nitrogen-doped laser reduced graphene films for wearable heating applications. The N-LrGO film was prepared by the facile and scalable low-temperature technique involving the combination of ultrasonic wet chemical doping and solid-state photo-irradiation. This novel technique was shown to the reduced sheet resistance of the LrGO by 50%, consequently lowering the required voltages for each desired saturation temperature in the N-LrGO heater and resulting in attractive performance features such as a high initial heating rate of 107 °C/s, low power demand of 30.07 W/m^2 °C and good temperature distribution. The heater also had good thermal, mechanical, and chemical stability. This, therefore, makes the N-LrGO heater safer and more compatible with the extended use of portable energy storage devices such as Li-ion batteries and thin-film supercapacitors. We also

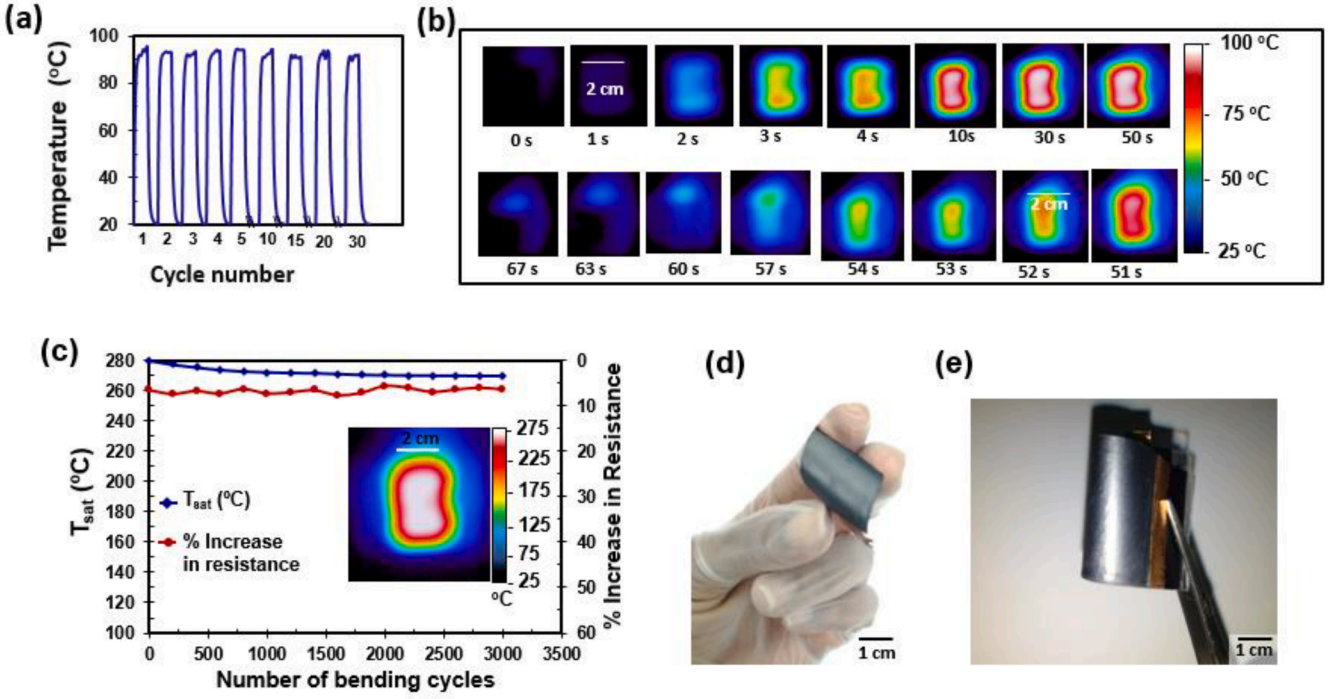

Fig. 7. Thermal and mechanical stability analyses (a) Thermal cycles of N-LrGO at 4.5 V; each cycle involved 50 s of heating and 30 s of cooling; only the first 5, 10th, 15th, 20th, and 30th cycles are shown; saturation temperature stays constant for all cycles. (b) Thermal images of the N-LrGO heater at different times during one 4.5 V thermal cycle; the entire heater surface is heated up by the 10th second and completely cool down by the 67th second. (c) Change in saturation temperature and heater resistance with the number of bending cycles; a thermal image of the heater is inserted showing good thermal distribution after 3000 bending cycles. Optical images of N-LrGO heater (d) twisted at an oblique angle (e) folded to an acute bending angle with no visible damages.

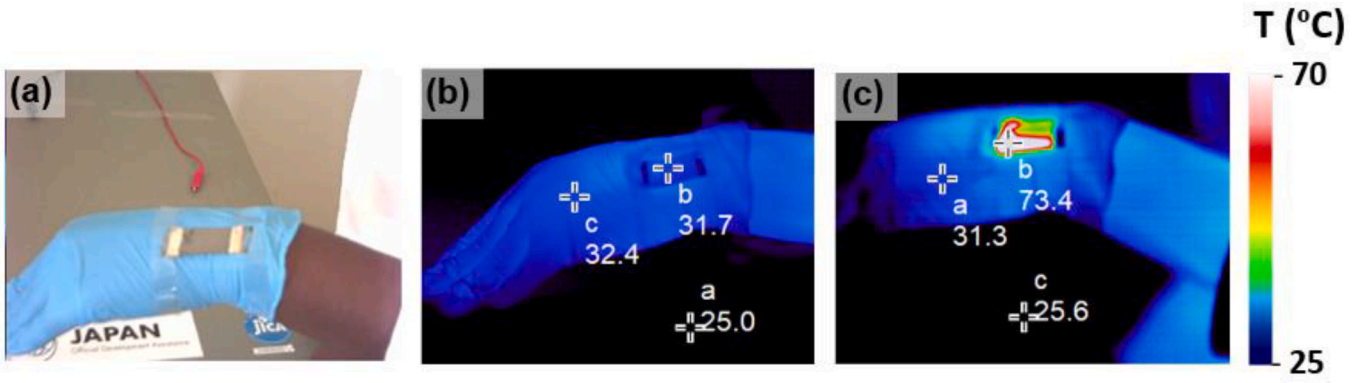

Fig. 8. Applying the N-LrGO heater as a thermotherapy patch. (a) Optical and (b) thermal images of the 1.5 by 2.5 cm^2 N-LrGO heater worn around a human wrist slightly tilted sideways with 0 V applied voltage and (c) 4 V applied voltage; A surface emissivity of 0.75 was used for image processing.

successfully applied the N-LrGO heater as a thermotherapy patch to showcase its applicability in next-generation wearable electronics.

CRediT authorship contribution statement

Sandra A.N. Tembei: Methodology, Investigation, Data curation, Writing - original draft. **Ahmed M.R. Fath El-Bab:** Writing - review & editing, Resources. **Amr Hessein:** Writing - review & editing, Visualization, Supervision. **Ahmed Abd El-Moneim:** Conceptualization, Resources, Supervision, Project administration.

Declaration of Competing Interest

The authors declare that they have no known competing financial interests or personal relationships that could have appeared to influence the work reported in this paper.

Acknowledgments

We also want to acknowledge the Japan International Co-operation Agency (JICA) for their reliable sponsorship of our work. This research was conducted as part of the research project: graphene center of excellence for energy and electronic applications (ID ¼ 31306) that is supported by the science and technology development fund (STDF) in Egypt.

Appendix A. Supplementary data

Supplementary data to this article can be found online at https://doi.org/10.1016/j.flatc.2020.100199.

References

[1] D. Janas, K.K. Koziol, A review of production methods of carbon nanotube and graphene thin films for electrothermal applications, Nanoscale 6 (6) (2014) 3037, https://doi.org/10.1039/c3nr05636h.
[2] S.-L. Jia, H.-Z. Geng, L. Wang, Y. Tian, C.-X. Xu, P.-P. Shi, Z.-Z. Gu, X.-S. Yuan, L.-C. Jing, Z.-Y. Guo, J. Kong, Carbon nanotube-based flexible electrothermal film heaters with a high heating rate, R. Soc. open sci. 5 (6) (2018) 172072, https://doi.org/10.1098/rsos.172072.
[3] M.R. Bobinger, F.J. Romero, A. Salinas-Castillo, M. Becherer, P. Lugli, D. P. Morales, N. Rodríguez, A. Rivadeneyra, Flexible and robust laser-induced graphene heaters photothermally scribed on bare polyimide substrates, Carbon 144 (2019) 116–126, https://doi.org/10.1016/j.carbon.2018.12.010.
[4] D. Sui, Y.i. Huang, L.u. Huang, J. Liang, Y. Ma, Y. Chen, Flexible and transparent electrothermal film heaters based on graphene materials, Small 7 (22) (2011) 3186–3192, https://doi.org/10.1002/smll.201101305.
[5] S.-Y. Lin, T.-Y. Zhang, Q.i. Lu, D.-Y. Wang, Y.i. Yang, X.-M. Wu, T.-L. Ren, High-performance graphene-based flexible heater for wearable applications, RSC Adv. 7 (43) (2017) 27001–27006, https://doi.org/10.1039/C7RA03181E.
[6] M.-S. Lee, K. Lee, S.-Y. Kim, H. Lee, J. Park, K.-H. Choi, H.-K. Kim, D.-G. Kim, D.-Y. Lee, SungWoo Nam, J.-U. Park, High-performance, transparent, and stretchable electrodes using graphene–metal nanowire hybrid structures, Nano Lett. 13 (6) (2013) 2814–2821, https://doi.org/10.1021/nl401070p.
[7] R. Wang, Z. Xu, J. Zhuang, Z. Liu, L.i. Peng, Z. Li, Y. Liu, W. Gao, C. Gao, Highly stretchable graphene fibers with ultrafast electrothermal response for low-voltage wearable heaters, Adv. Electron. Mater. 3 (2) (2017) 1600425, https://doi.org/10.1002/aelm.201600425.
[8] B.W. An, E.-J. Gwak, K. Kim, Y.-C. Kim, J. Jang, J.-Y. Kim, J.-U. Park, Stretchable, transparent electrodes as wearable heaters using nanotrough networks of metallic glasses with superior mechanical properties and thermal stability, Nano Lett. 16 (1) (2016) 471–478, https://doi.org/10.1021/acs.nanolett.5b04134.
[9] C. Celle, C. Mayousse, E. Moreau, H. Basti, A. Carella, J.-P. Simonato, Highly flexible transparent film heaters based on random networks of silver nanowires, Nano Res. 5 (6) (2012) 427–433, https://doi.org/10.1007/s12274-012-0225-2.
[10] S. Hong, H. Lee, J. Lee, J. Kwon, S. Han, Y.D. Suh, H. Cho, J. Shin, J. Yeo, S.H. Ko, Highly stretchable and transparent metal nanowire heater for wearable electronics applications, Adv. Mater. 27 (32) (2015) 4744–4751, https://doi.org/10.1002/adma.201500917.
[11] E.-H. Ko, H.-J. Kim, S.-M. Lee, T.-W. Kim, H.-K. Kim, Stretchable Ag electrodes with mechanically tunable optical transmittance on wavy-patterned PDMS substrates, Sci Rep 7 (1) (2017), https://doi.org/10.1038/srep4673910.1038/srep46739.
[12] E.-H. Ko, H.-J. Kim, S.-J. Lee, J.-H. Lee, H.-K. Kim, Nano-sized Ag inserted into ITO films prepared by continuous roll-to-roll sputtering for high-performance, flexible, transparent film heaters, RSC Adv. 6 (52) (2016) 46634–46642, https://doi.org/10.1039/C6RA08704C.
[13] L.R. Pahalagedara, I. Siriwardane, N.D. Tissera, R.N. Wijesena, K.M.N. de Silva, Carbon black functionalized stretchable conductive fabrics for wearable heating applications, RSC Adv. 7 (31) (2017) 19174–19180, https://doi.org/10.1039/C7RA02184D.
[14] Y. Atwa, N. Maheshwari, I.A. Goldthorpe, Silver nanowire coated threads for electrically conductive textiles, J. Mater. Chem. C 3 (16) (2015) 3908–3912, https://doi.org/10.1039/C5TC00380F.
[15] S.u. Ding, J. Jiu, Y. Gao, Y. Tian, T. Araki, T. Sugahara, S. Nagao, M. Nogi, H. Koga, K. Suganuma, H. Uchida, One-step fabrication of stretchable copper nanowire conductors by a fast photonic sintering technique and its application in wearable devices, ACS Appl. Mater. Interfaces 8 (9) (2016) 6190–6199, https://doi.org/10.1021/acsami.5b10802.
[16] J. Yan, Y.G. Jeong, Highly elastic and transparent multiwalled carbon nanotube/polydimethylsiloxane bilayer films as electric heating materials, Mater. Des. 86 (2015) 72–79, https://doi.org/10.1016/j.matdes.2015.07.089.
[17] R. Zhou, P. Li, Z. Fan, D. Du, J. Ouyang, Stretchable heaters with composites of an intrinsically conductive polymer, reduced graphene oxide and an elastomer for wearable thermotherapy, J. Mater. Chem. C 5 (6) (2017) 1544–1551, https://doi.org/10.1039/C6TC04849H.
[18] S. Sharifi, S. Behzadi, S. Laurent, M. Laird Forrest, P. Stroeve, M. Mahmoudi, Toxicity of nanomaterials, Chem. Soc. Rev. 41 (6) (2012) 2323–2343, https://doi.org/10.1039/C1CS15188F.
[19] G.W. Hunter, S. Akbar, S. Bhansali, M. Daniele, P.D. Erb, K. Johnson, C.-C. Liu, D. Miller, O. Oralkan, P.J. Hesketh, P. Manickam, R.L. Vander Wal, Editors' choice—critical review—a critical review of solid state gas sensors, J. Electrochem. Soc. 167 (3) (2020) 037570, https://doi.org/10.1149/1945-7111/ab729c.
[20] M. Gamil, H. Nageh, I. Bkrey, S. Sayed, O. Tabata, A.A. El-Moneim, Graphene-based strain gauge on a flexible substrate, Sens. Mater. 26 (2014) 11.
[21] S. Sayed, High Performance Carbon Monoxide Gas Sensor based on Graphene, Int. J. Eng. Res. 4 (n.d.) 6.
[22] S. Sayed, M. Gamil, A.M.R. Fath El-Bab, A.A.E.M. Abd Elmoneim, LASER reduced graphene on flexible substrate for strain sensing applications: temperature Effect on Gauge Factor, KEM 644 (2015) 115–119, https://doi.org/10.4028/www.scientific.net/KEM.644.115.
[23] E. Ghoniem, S. Mori, A. Abdel-Moniem, Low-cost flexible supercapacitors based on laser reduced graphene oxide supported on polyethylene terephthalate substrate, J. Power Sources 324 (2016) 272–281, https://doi.org/10.1016/j.jpowsour.2016.05.069.

[24] R. You, Y.-Q. Liu, Y.-L. Hao, D.-D. Han, Y.-L. Zhang, Z. You, Laser fabrication of graphene-based flexible electronics, Adv. Mater. 32 (15) (2020) 1901981, https://doi.org/10.1002/adma.201901981.
[25] Y.-Q. Liu, J.-W. Mao, Z.-D. Chen, D.-D. Han, Z.-Z. Jiao, J.-N. Ma, H.-B. Jiang, H. yang, Three-dimensional micropatterning of graphene by femtosecond laser direct writing technology, Opt. Lett. 45 (1) (2020) 113, https://doi.org/10.1364/OL.45.000113.
[26] M. Gamil, O. Tabata, K. Nakamura, A.M.R.F. El-Bab, A.A. El-Moneim, Investigation of a new high sensitive micro-electromechanical strain gauge sensor based on graphene piezoresistivity, KEM 605 (2014) 207–210, https://doi.org/10.4028/www.scientific.net/KEM.605.207.
[27] A. Datcu, L. Duta, A. Pérez del Pino, C. Logofatu, C. Luculescu, A. Duta, D. Perniu, E. György, One-step preparation of nitrogen doped titanium oxide/Au/reduced graphene oxide composite thin films for photocatalytic applications, RSC Adv. 5 (61) (2015) 49771–49779, https://doi.org/10.1039/C5RA07853A.
[28] L.i. Guo, Y.-L. Zhang, D.-D. Han, H.-B. Jiang, D. Wang, X.-B. Li, H. Xia, J. Feng, Q.-D. Chen, H.-B. Sun, Laser-mediated programmable N doping and simultaneous reduction of graphene oxides, Adv. Opt. Mater. 2 (2) (2014) 120–125.
[29] B.D. Ryu, N. Han, M. Han, S. Chandramohan, Y.J. Park, K.B. Ko, J.B. Park, T. V. Cuong, C.-H. Hong, Stimulated N-doping of reduced graphene oxide on GaN under excimer laser reduction process, Mater. Lett. 116 (2014) 412–415, https://doi.org/10.1016/j.matlet.2013.11.072.
[30] A.A. El-Moneim, J. Bhattarai, Z. Kato, K. Izumiya, N. Kumagai, K. Hashimoto, Mn-Mo-Sn oxide anodes for oxygen evolution in seawater electrolysis for hydrogen production, ECS Trans. 25 (40) (2010) 127–137, https://doi.org/10.1149/1.3422589.
[31] K. Rathinam, S.P. Singh, Y. Li, R. Kasher, J.M. Tour, C.J. Arnusch, Polyimide derived laser-induced graphene as adsorbent for cationic and anionic dyes, Carbon 124 (2017) 515–524, https://doi.org/10.1016/j.carbon.2017.08.079.
[32] C. Zhang, Y. Xie, C. Zhang, J. Lin, Upgrading coal to multifunctional graphene-based materials by direct laser scribing, Carbon 153 (2019) 585–591, https://doi.org/10.1016/j.carbon.2019.07.070.
[33] T.-Y. Zhang, H.-M. Zhao, D.-Y. Wang, Q. Wang, Y.u. Pang, N.-Q. Deng, H.-W. Cao, Y.i. Yang, T.-L. Ren, A super flexible and custom-shaped graphene heater, Nanoscale 9 (38) (2017) 14357–14363, https://doi.org/10.1039/C7NR02219K.
[34] X. Wang, G. Sun, P. Routh, D.-H. Kim, W. Huang, P. Chen, Heteroatom-doped graphene materials: syntheses, properties and applications, Chem. Soc. Rev. 43 (20) (2014) 7067–7098, https://doi.org/10.1039/C4CS00141A.
[35] T. Wu, H. Shen, L. Sun, B. Cheng, B. Liu, J. Shen, Nitrogen and boron doped monolayer graphene by chemical vapor deposition using polystyrene, urea and boric acid, New J. Chem. 36 (6) (2012) 1385, https://doi.org/10.1039/c2nj40068e.
[36] M. Son, S.-S. Chee, S.-Y. Kim, W. Lee, Y.H. Kim, B.-Y. Oh, J.Y. Hwang, B.H. Lee, M.-H. Ham, High-quality nitrogen-doped graphene films synthesized from pyridine via two-step chemical vapor deposition, Carbon 159 (2020) 579–585, https://doi.org/10.1016/j.carbon.2019.12.095.
[37] W. Zheng, Y. Zhang, K. Niu, T. Liu, K. Bustillo, P. Ercius, D. Nordlund, J. Wu, H. Zheng, X. Du, Selective nitrogen doping of graphene oxide by laser irradiation for enhanced hydrogen evolution activity, Chem. Commun. 54 (97) (2018) 13726–13729, https://doi.org/10.1039/C8CC07725H.
[38] Z. Mou, X. Chen, Y. Du, X. Wang, P. Yang, S. Wang, Forming mechanism of nitrogen doped graphene prepared by thermal solid-state reaction of graphite oxide and urea, Appl. Surf. Sci. 258 (5) (2011) 1704–1710, https://doi.org/10.1016/j.apsusc.2011.10.019.
[39] G.H. Jun, S.H. Jin, B. Lee, B.H. Kim, W.-S. Chae, S.H. Hong, S. Jeon, Enhanced conduction and charge-selectivity by N-doped graphene flakes in the active layer of bulk-heterojunction organic solar cells, Energy Environ. Sci. 6 (10) (2013) 3000, https://doi.org/10.1039/c3ee40963e.
[40] P. Wu, Z. Cai, Y. Gao, H. Zhang, C. Cai, Enhancing the electrochemical reduction of hydrogen peroxide based on nitrogen-doped graphene for measurement of its releasing process from living cells, Chem. Commun. 47 (40) (2011) 11327, https://doi.org/10.1039/c1cc14419g.
[41] W. Zeng, X.-M. Tao, S. Lin, C. Lee, D. Shi, K.-h. Lam, B. Huang, Q. Wang, Y. Zhao, Defect-engineered reduced graphene oxide sheets with high electric conductivity and controlled thermal conductivity for soft and flexible wearable thermoelectric generators, Nano Energy 54 (2018) 163–174, https://doi.org/10.1016/j.nanoen.2018.10.015.
[42] M. Stoppa, A. Chiolerio, Wearable electronics and smart textiles: a critical review, Sensors 14 (7) (2014) 11957–11992, https://doi.org/10.3390/s140711957.
[43] S. Eigler, M. Enzelberger-Heim, S. Grimm, P. Hofmann, W. Kroener, A. Geworski, C. Dotzer, M. Röckert, J. Xiao, C. Papp, O. Lytken, H.-P. Steinrück, P. Müller, A. Hirsch, Wet chemical synthesis of graphene, Adv. Mater. 25 (26) (2013) 3583–3587, https://doi.org/10.1002/adma.201300155.
[44] A. Hessein, F. Wang, H. Masai, K. Matsuda, A.A. El-Moneim, One-step fabrication of copper sulfide nanoparticles decorated on graphene sheets as highly stable and efficient counter electrode for CdS-sensitized solar cells, Jpn. J. Appl. Phys. 55 (11) (2016) 112301, https://doi.org/10.7567/JJAP.55.112301.
[45] S. Park, J. An, J.R. Potts, A. Velamakanni, S. Murali, R.S. Ruoff, Hydrazine-reduction of graphite- and graphene oxide, Carbon 49 (9) (2011) 3019–3023, https://doi.org/10.1016/j.carbon.2011.02.071.
[46] E. Kymakis, C. Petridis, T.D. Anthopoulos, E. Stratakis, Laser-assisted reduction of graphene oxide for flexible, large-area optoelectronics, IEEE J. Select. Topics Quantum Electron. 20 (1) (2014) 106–115, https://doi.org/10.1109/JSTQE.2013.2273414.
[47] L.M. Malard, M.A. Pimenta, G. Dresselhaus, M.S. Dresselhaus, Raman spectroscopy in graphene, Phys. Rep. 473 (5-6) (2009) 51–87, https://doi.org/10.1016/j.physrep.2009.02.003.
[48] R. Trusovas, G. Račiukaitis, G. Niaura, J. Barkauskas, G. Valušis, R. Pauliukaite, Recent Advances in laser utilization in the chemical modification of graphene oxide and its applications, Adv. Opt. Mater. 4 (1) (2016) 37–65, https://doi.org/10.1002/adom.201500469.
[49] Z. Lin, G.H. Waller, Y. Liu, M. Liu, C.-P. Wong, Simple preparation of nanoporous few-layer nitrogen-doped graphene for use as an efficient electrocatalyst for oxygen reduction and oxygen evolution reactions, Carbon 53 (2013) 130–136, https://doi.org/10.1016/j.carbon.2012.10.039.
[50] H.L. Poh, F. Šaněk, A. Ambrosi, G. Zhao, Z. Sofer, M. Pumera, Graphenes prepared by Staudenmaier, Hofmann and Hummers methods with consequent thermal exfoliation exhibit very different electrochemical properties, Nanoscale 4 (11) (2012) 3515, https://doi.org/10.1039/c2nr30490b.
[51] Y. Huang, L. Zeng, C. Liu, D. Zeng, Z. Liu, X. Liu, X. Zhong, W. Guo, L. Li, Laser direct writing of heteroatom (N and S)-doped graphene from a polybenzimidazole ink donor on polyethylene terephthalate polymer and glass substrates, Small 14 (44) (2018) 1803143, https://doi.org/10.1002/smll.201803143.
[52] X.-Y. Fu, D.-L. Chen, Y. Liu, H.-B. Jiang, H. Xia, H. Ding, Y.-L. Zhang, Laser reduction of nitrogen-rich carbon nanoparticles@graphene oxides composites for high rate performance supercapacitors, ACS Appl. Nano Mater. 1 (2) (2018) 777–784, https://doi.org/10.1021/acsanm.7b00225.
[53] D.-D. Han, Y.-L. Zhang, Y. Liu, Y.-Q. Liu, H.-B. Jiang, B. Han, X.-Y. Fu, H. Ding, H.-L. Xu, H.-B. Sun, Bioinspired graphene actuators prepared by unilateral UV irradiation of graphene oxide papers, Adv. Funct. Mater. 25 (28) (2015) 4548–4557, https://doi.org/10.1002/adfm.201501511.
[54] D.-D. Han, Y.-L. Zhang, H.-B. Jiang, H. Xia, J. Feng, Q.-D. Chen, H.-L. Xu, H.-B. Sun, Moisture-responsive graphene paper prepared by self-controlled photoreduction, Adv. Mater. 27 (2) (2015) 332–338, https://doi.org/10.1002/adma.201403587.
[55] A. Morais, J.P.C. Alves, F.A.S. Lima, M. Lira-Cantu, A.F. Nogueira, Enhanced photovoltaic performance of inverted hybrid bulk-heterojunction solar cells using TiO2/reduced graphene oxide films as electron transport layers, J. Photon. Energy 5 (1) (2015) 057408, https://doi.org/10.1117/1.JPE.5.057408.
[56] L.i. Sun, L. Wang, C. Tian, T. Tan, Y. Xie, K. Shi, M. Li, H. Fu, Nitrogen-doped graphene with high nitrogen level via a one-step hydrothermal reaction of graphene oxide with urea for superior capacitive energy storage, RSC Adv. 2 (10) (2012) 4498, https://doi.org/10.1039/c2ra01367c.
[57] S. He, F. Biedermann, N. Vankova, L. Zhechkov, T. Heine, R.E. Hoffman, A. De Simone, T.T. Duignan, W.M. Nau, Cavitation energies can outperform dispersion interactions, Nature Chem 10 (12) (2018) 1252–1257, https://doi.org/10.1038/s41557-018-0146-0.
[58] B. Gupta, N. Kumar, K. Panda, V. Kanan, S. Joshi, I. Visoly-Fisher, Role of oxygen functional groups in reduced graphene oxide for lubrication, Sci Rep 7 (1) (2017), https://doi.org/10.1038/srep45030.
[59] R. Yadav, C.K. Dixit, Synthesis, characterization and prospective applications of nitrogen-doped graphene: a short review, J. Sci.: Adv. Mater. Devices 2 (2) (2017) 141–149, https://doi.org/10.1016/j.jsamd.2017.05.007.
[60] M. Yang, Z. Zhang, X. Zhu, X. Men, G. Ren, In situ reduction and functionalization of graphene oxide to improve the tribological behavior of a phenol formaldehyde composite coating, Friction 3 (1) (2015) 72–81, https://doi.org/10.1007/s40544-015-0076-4.
[61] T. Schiros, D. Nordlund, L. Pálová, D. Prezzi, L. Zhao, K.S. Kim, U. Wurstbauer, C. Gutiérrez, D. Delongchamp, C. Jaye, D. Fischer, H. Ogasawara, L.G. M. Pettersson, D.R. Reichman, P. Kim, M.S. Hybertsen, A.N. Pasupathy, Connecting dopant bond type with electronic structure in N-doped graphene, Nano Lett. 12 (8) (2012) 4025–4031, https://doi.org/10.1021/nl301409h.
[62] D. Das, S. Kim, K.-R. Lee, A.K. Singh, Li diffusion through doped and defected graphene, Phys. Chem. Chem. Phys. 15 (36) (2013) 15128, https://doi.org/10.1039/c3cp52891j.
[63] X.-K. Kong, Q.-W. Chen, Improved performance of graphene doped with pyridinic N for Li-ion battery: a density functional theory model, Phys. Chem. Chem. Phys. 15 (31) (2013) 12982, https://doi.org/10.1039/c3cp51987b.
[64] K.-Y. Shin, J.-Y. Hong, S. Lee, J. Jang, High electrothermal performance of expanded graphite nanoplatelet-based patch heater, J. Mater. Chem. 22 (44) (2012) 23404, https://doi.org/10.1039/c2jm34196d.
[65] D. Kim, L. Zhu, D.-J. Jeong, K. Chun, Y.-Y. Bang, S.-R. Kim, J.-H. Kim, S.-K. Oh, Transparent flexible heater based on hybrid of carbon nanotubes and silver nanowires, Carbon 63 (2013) 530–536, https://doi.org/10.1016/j.carbon.2013.07.030.
[66] M. Tian, Y. Hao, L. Qu, S. Zhu, X. Zhang, S. Chen, Enhanced electrothermal efficiency of flexible graphene fabric Joule heaters with the aid of graphene oxide, Mater. Lett. 234 (2019) 101–104, https://doi.org/10.1016/j.matlet.2018.09.078.
[67] J. Xie, W. Pan, Y. Chen, Z. Guo, Preparation of polypyrrole coated on Polyester Cleanroom Wiper as heater device, J. Eng. Fibers Fabr. 15 (2020), https://doi.org/10.1177/1558925020925408, 155892502092540.
[68] Y. Zhang, H. Liu, L. Tan, Y. Zhang, K. Jeppson, B. Wei, J. Liu, Properties of undoped few-layer graphene-based transparent heaters, Materials 13 (1) (2020) 104, https://doi.org/10.3390/ma13010104.
[69] Y. Hao, M. Tian, H. Zhao, L. Qu, S. Zhu, X. Zhang, S. Chen, K.e. Wang, J. Ran, High efficiency electrothermal graphene/tourmaline composite fabric joule heater with durable abrasion resistance via a spray coating route, Ind. Eng. Chem. Res. 57 (40) (2018) 13437–13448, https://doi.org/10.1021/acs.iecr.8b03628.
[70] B.o. Wang, H. Cheng, J. Zhu, Y. Yuan, C. Wang, A flexible and stretchable polypyrrole/knitted cotton for electrothermal heater, Org. Electron. 85 (2020) 105819, https://doi.org/10.1016/j.orgel.2020.105819.

[71] S. Lee, D. Jang, Y.S. Chung, S. Lee, Cost-effective and highly efficient surface heating elements using high thermal conductive carbon fibers, Compos. A Appl. Sci. Manuf. 137 (2020) 105992, https://doi.org/10.1016/j.compositesa:2020.105992.

[72] X.-Y. Fu, Z.-D. Chen, D.-D. Han, Y.-L. Zhang, H. Xia, H.-B. Sun, Laser fabrication of graphene-based supercapacitors, Photon. Res. 8 (4) (2020) 577, https://doi.org/10.1364/PRJ.382401.

[73] K.e. Wang, Z. Zhou, Y. Wang, Flexible electrothermal polymer film based on reduced graphene oxide–water polyurethane, Mod. Phys. Lett. B 34 (25) (2020) 2050265, https://doi.org/10.1142/S0217984920502656.

[74] X. Meng, T. Chen, Y. Li, S. Liu, H. Pan, Y. Ma, Z. Chen, Y. Zhang, S. Zhu, Assembly of carbon nanodots in graphene-based composite for flexible electro-thermal heater with ultrahigh efficiency, Nano Res. 12 (10) (2019) 2498–2508, https://doi.org/10.1007/s12274-019-2476-7.

[75] P. Sarzi-Puttini, M.A. Cimmino, R. Scarpa, R. Caporali, F. Parazzini, A. Zaninelli, F. Atzeni, B. Canesi, Osteoarthritis: an overview of the disease and its treatment strategies, Semin. Arthritis Rheum. 35 (1) (2005) 1–10, https://doi.org/10.1016/j.semarthrit.2005.01.013.

[76] S. Michlovitz, L. Hun, G.N. Erasala, D.A. Hengehold, K.W. Weingand, Continuous low-level heat wrap therapy is effective for treating wrist pain11A commercial party with a direct financial interest in the results of the research supporting this article has conferred or will confer a financial benefit on the author or/or more of the authors. Arch. Phys. Med. Rehabil. 85 (9) (2004) 1409–1416, https://doi.org/10.1016/j.apmr.2003.10.016.